



Tunable auxeticity in hydrogenated carbon nanotube origami metamaterial

Jun Cai, Benyamin Shahryari, and Abdolhamid Akbarzadeh*^{1b}

Impact statement

Carbon nanotubes (CNTs), the classic one-dimensional material, were uncovered in 1991 and reported to be made out of a single graphene layer later in 1993. Since these discoveries, the carbon-based materials have attracted intensive research interest due to their outstanding thermo-electro-mechanical properties. To expand their range of applications and overcome their shortcomings such as brittleness and low-dimensional feature, many engineering strategies have been proposed to modify their properties. Inspired by the ancient art of paper folding, we first construct the CNT origami with a Miura-ori tessellation via surface functionalization using hydrogen atoms and then resort to molecular dynamics simulation, theoretical analysis, and experimental test to demonstrate that the origami strategy can provide a platform for designing CNTs with enhanced stretchability, high strength, and scale-independent strain-dependent negative Poisson's ratio. More specifically, the mechanical properties of CNT origamis can be tuned and programmed by altering the folding width and topological parameters of Miura-ori patterns. Our findings provide new opportunities for the realization of low-dimensional architected nanomaterials capable of achieving tunable mechanical properties and auxeticity.

Inspired by the origami architecture and the progress in the functionalization of carbon-based nanomaterials, we design a carbon nanotube origami (CNT-O) metamaterial with the assistance of hydrogenation and by utilizing molecular dynamics simulation. The mechanical properties, including stiffness, ultimate strength, failure strain, and Poisson's ratio, are systematically studied. Our findings show that the mechanical properties of CNT-O can be tuned and programmed by altering the underlying topological parameters and adopting surface functionalization. We resort to computational simulation, theoretical analysis, and experimentation to demonstrate that an extremely broad range of strain-dependent and scale-independent negative Poisson's ratio can be achieved for nanoarchitected metamaterials, mainly driven by the kinematics of the folding/unfolding in origamis. The proposed origami strategy imparts a platform for designing the next generation of low-dimensional nanomaterials (e.g., graphene and CNT) with highly tunable auxeticity.

Introduction

Carbon nanotubes (CNTs) and graphene, the classic low-dimensional nanomaterial, have attracted intensive research interest owing to their outstanding features,^{1–4} such as excellent mechanical strength and stiffness,^{5,6} ultrahigh thermal conductivity,⁷ chirality-dependent electrical conductivity,^{8,9} unique optoelectronic characteristics,¹⁰ and larger specific surface areas.¹¹ However, the brittle nature and low-dimensional features of such carbon-based nanomaterials (e.g., graphene, CNT, and fullerene) hamper their applications, for example, in wearable and flexible electronics.^{12,13} Many strategies have been proposed to modify the properties and overcome the shortcomings of graphene/CNT, such as the lattice-like nanotruss CNT networks by linking CNTs covalently,¹² bioinspired fibrous/helical CNTs,¹⁴ CNT bundles,¹⁵ CNT-pillared graphene network,¹⁶ three-dimensional (3D)

graphene foams,^{17–19} annealing-processed 3D disordered graphene networks,²⁰ and paper-cutting-inspired graphene/CNT kirigami.^{13,21} However, there are issues that are required to be addressed in the previously mentioned advanced nanomaterials. For example, the lattice-like CNT metamaterials and bioinspired fibrous/helical CNTs are still brittle with limited elasticity and the topological defects in the linkage of CNTs decrease their strength.¹² The stretchability of a CNT is improved significantly by introducing kirigami patterns, however, at the cost of reducing its stiffness and strength.¹³

Origami, the ancient Chinese and Japanese art of paper folding,²² not only results in interesting architectures,^{23–26} but also enables a design platform for developing advanced metamaterials with novel mechanical properties, such as increased stretchability,²⁷

Jun Cai, Department of Bioresource Engineering, McGill University, Montreal, QC, Canada
 Benyamin Shahryari, Department of Bioresource Engineering, McGill University, Montreal, QC, Canada
 Abdolhamid Akbarzadeh, Department of Bioresource Engineering, McGill University, Montreal, QC, Canada; Department of Mechanical Engineering, McGill University, Montreal, QC, Canada; hamid.akbarzadeh@mcgill.ca
 *Corresponding author
 doi:10.1557/s43577-023-00545-0



negative Poisson's ratio,^{22,28} negative coefficient of thermal expansion,²⁹ multistability,³⁰ and zero/negative incremental stiffness.^{31,32} Owing to the presence of creases in the origami-inspired metamaterials, the entire architecture can be folded and unfolded to obtain deployable structures;²⁸ the overall structural performance of origami is dominated by the underlying architecture-induced kinematic deformation modes.²² Here, we construct the CNT origami (CNT-O) with a Miura-ori tessellation,²² and combine molecular dynamics (MD) simulation and experimentation to demonstrate that the origami design can impart a strategy for developing CNT-based metamaterials with enhanced stretchability, high strength, and negative Poisson's ratio (i.e., auxeticity). To achieve this aim, we form the CNT-O via surface functionalization with the assistance of hydrogen atoms in MD simulation, which is a feasible way to realize nanomaterials with tunable properties. Significant progress in the hydrogenation of CNT and graphene has been achieved through experimentation^{33–38} (see Supplementary information S1 for more information). For example, the hydrogenation of a CNT has been realized via a modified Birch reduction method³⁶ or using a glow-discharge approach.³⁵ Meanwhile, the hydrogenation mapping such as origami patterning on graphene can be precisely controlled using a photoresist mask.³⁹ The subsequent imaging using fluorescence quenching microscopy (FQM) has revealed that this technology can realize complicated hydrogenation patterns on nanomaterials.³⁹ However, due to the curved surface of the CNT, achieving a precise functionalization mapping remains a challenge with this approach, and new or modified technologies are yet to be developed to make desired hydrogenation patterns on freeform surfaces.

In this article, the hydrogenated CNT-O is virtually formed in a MD simulation, followed by a theoretical analysis and mechanical testing on prototypes on mesoscale counterparts made out of conventional cellulose-based papers. Our results indicate that the stretchability and the strength of CNT-O can be increased simultaneously in some cases (i.e., samples with large folding widths and enhanced number of cells along the circumference of CNT-O), and a variable strain-dependent negative Poisson's ratio can be attained. All of the mechanical properties of the nanoarchitected origami can be controlled by tuning geometrical parameters. Moreover, we demonstrate that the folding/unfolding of CNT-O enables tunability of the negative Poisson's ratio, opening avenues for the realization of a new class of nonporous auxetic nanomaterials.

Modeling and methods

MD simulation

MD simulation is conducted using the large-scale atomic molecular massively parallel simulator (LAMMPS)⁴⁰ to study the surface functionalization and mechanical responses of CNT-O. The Open Visualization Tool (OVITO)⁴¹ is employed to visualize the evolution of atomic structures.

AIREBO⁴² potential function is used to describe C–C and C–H interatomic interactions. The cutoff distance between C–C is set at 2.0 Å to avoid the spurious strengthening effect.^{12,13,27} Periodic boundary condition is applied along the origami carbon nanotube axial direction. To transform a cylindrical CNT to a folded origami configuration, the surface functionalization is performed by placing hydrogen atoms approximately in 1.1 Å distance from the adjacent carbon atom^{27,43} (Figure 1a). Initially, energy minimization is performed by a conjugate gradient algorithm. Then, the engineered hydrogenated CNT is relaxed in the canonical ensemble (NVT) for 100 picoseconds (ps) and the isothermal-isobaric ensemble (NPT) for 3500 ps with a time step of 1 femtosecond (fs). A low temperature of 1 K is set to limit the influence of thermal fluctuation.¹⁵ A stable CNT-O with minimal potential energy can be obtained after full relaxation, as shown in Figure 2a. After obtaining the stable CNT-O nanostructures, the samples are subjected to a homogeneous tensile/compressive deformation by rescaling the vertical coordinates of all atoms in the simulation box to study their mechanical responses. The strain rate is set at $1 \times 10^{-9} \text{ s}^{-1}$. The axial stress is calculated by averaging the virial stress of all atoms in the system as¹⁴

$$\sigma_{ij} = \frac{1}{V_0} \sum_{\gamma=1}^n S_{ij}^{\gamma}, \quad 1$$

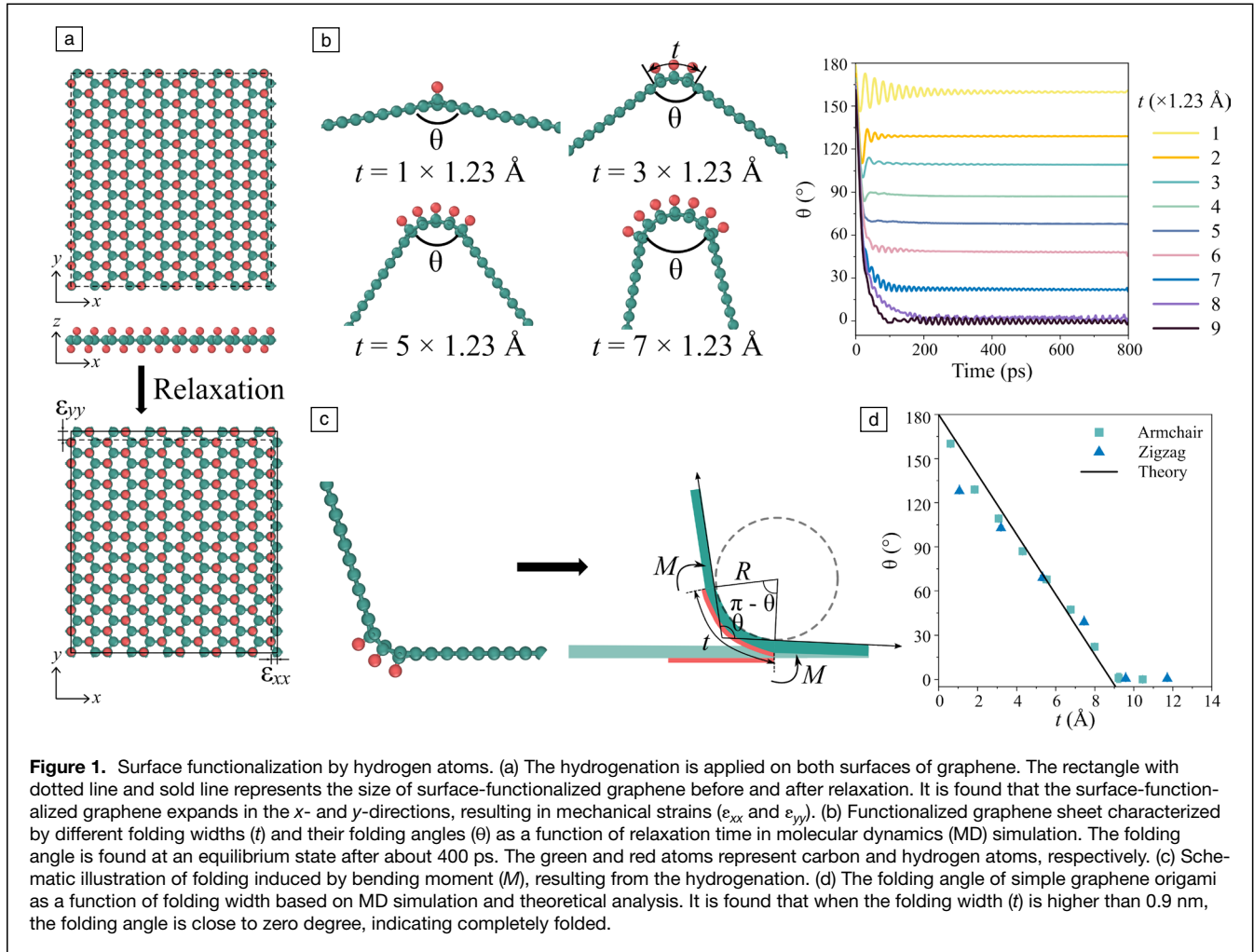
where V_0 is the initial volume of the material; S_{ij}^{γ} is the stress tensor for atom γ ; and i and j denote the indices associated with axes of the Cartesian coordinate system. The atomic stress of individual carbon atom α in the CNT-O nanostructure is calculated by¹⁴

$$S_{ij}^{\alpha} = \frac{1}{2} m^{\alpha} v_i^{\alpha} v_j^{\alpha} + \sum_{\beta=1}^n r_{\alpha\beta}^j f_{\alpha\beta}^i, \quad 2$$

where m^{α} and v^{α} represent the mass and velocity of atom α ; $r_{\alpha\beta}$ and $f_{\alpha\beta}$ are the distance and force between atoms α and β .

Surface functionalization mechanism

We use a simple 2D carbon-based nanomaterial (i.e., graphene) functionalized by hydrogen atoms to illustrate the mechanism of surface functionalization (Figure 1a–b). The hydrogenation generates an sp^3 -H bond between hydrogen and carbon atoms, which induces accumulated distortion, transforming a 2D graphene sheet into a 3D graphene origami.^{27,43} The folding angle (θ) of hydrogenated graphene reaches an equilibrium state after about 400 ps (Figure 1b); folding angle at equilibrium enhances with the increased number of hydrogenated rows (i.e., folding width, t).^{27,43} The definition of the folding width (t) can be found in Supplementary information Figure S1. It is found that when the hydrogen atoms are applied on both sides of the graphene (Figure 1a), the functionalized graphene expands in the in-plane directions



resulting in mechanical strains (ϵ_{xx} and ϵ_{yy}),⁴⁴ which exhibit an approximately linear relationship with hydrogenation density (ρ) (Supplementary information Figure S2). In the case of hydrogenation density $\rho = 100\%$ (the surface functionalization is applied on both sides of the graphene surface; all the carbon atoms are hydrogenated [see Figure 1a and Supplementary information Figure S2]), the hydrogenation-induced in-plane mechanical strains are around $\epsilon_{\rho=100\%} = 0.0278$. Then, the hydrogenation-induced surface force, resulting in the in-plane expansion of the graphene sheet, can be given by

$$F = E\epsilon(\rho)c, \quad 3$$

where $E \approx 1095$ GPa is the effective stiffness of pristine graphene within a small range of mechanical strain (~ 0.03) and $c = 0.335$ nm is the effective thickness of graphene; $\epsilon(\rho) = \rho\epsilon_{\rho=100\%}$ is the mechanical strain induced by surface functionalization with a hydrogenation density ρ . If the hydrogen atoms are applied only on one surface (Figure 1b), a bending moment (M) can be generated by the surface stress,^{44,45} inducing the graphene folding, which is given by (Figure 1c)

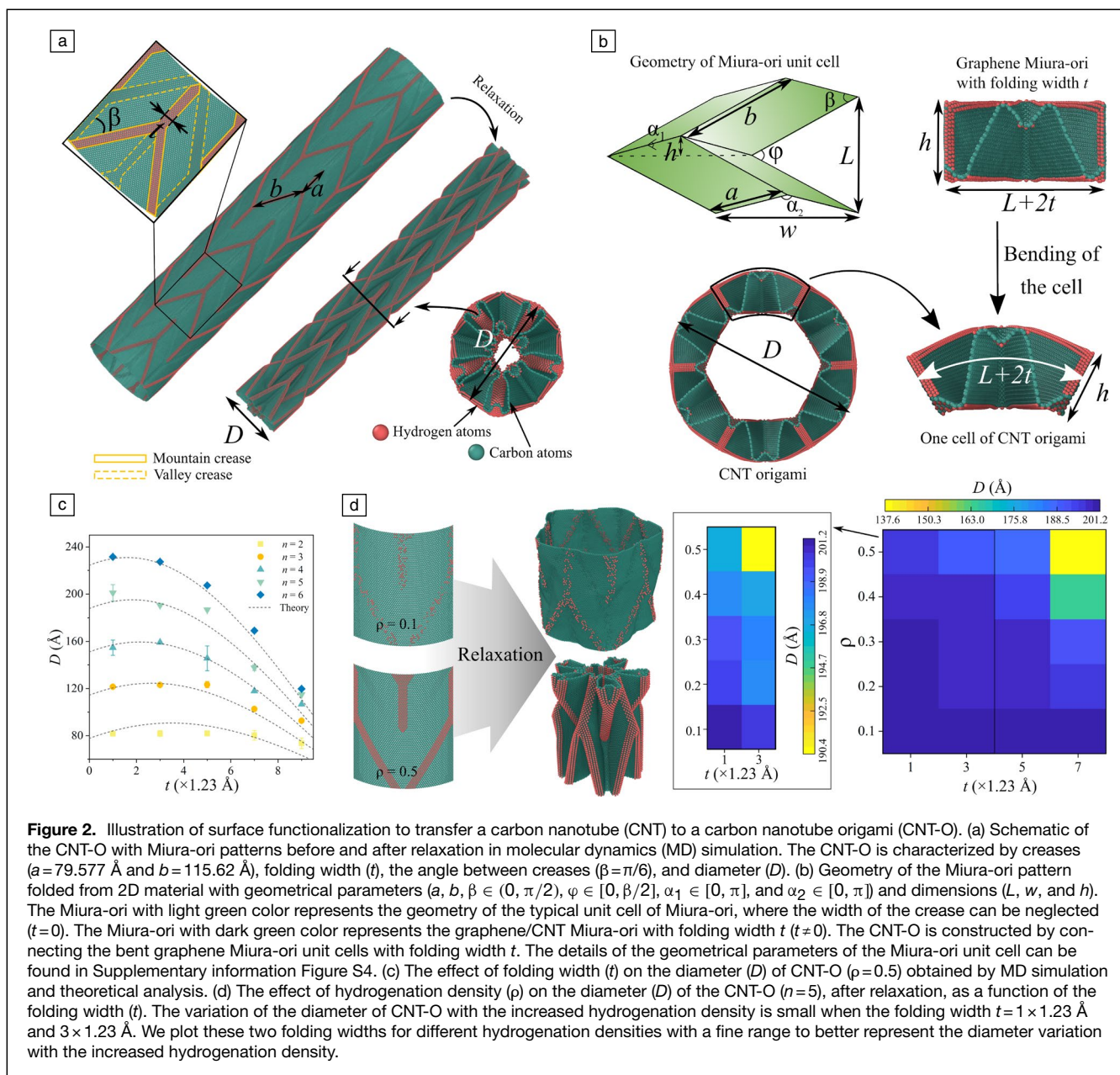
$$M = \frac{Fc}{2} = \frac{E\epsilon(\rho)c^2}{2}. \quad 4$$

Given the bending/flexural modulus of the pristine graphene ($K \approx 0.24$ nN·nm),^{46–48} based on the classic plate theory, the curvature of the cylindrical folding and the associated folding angle (θ) can be given by⁴⁴

$$\frac{1}{R} = \frac{M}{K} = \frac{E\epsilon(\rho)c^2}{2K} \quad 5a$$

$$\theta = \pi - \frac{t}{R} = \pi - \frac{E\epsilon(\rho)c^2t}{2K}. \quad 5b$$

As shown in Figure 1d, the hydrogenation-induced folding angles calculated by theory based on Equation 5b fit well with the MD simulation results; the folding angle decreases when the folding width increases. It is worth mentioning that in this study the highest hydrogenation density on one side of the surface is $\rho = 0.5$, and the largest folding width is $t = 9 \times 1.23$ Å. When the hydrogenation density is much higher than 0.5, the functionalized graphene cannot reach a stable state during the relaxation process in MD simulation, and forms defects on the surface of graphene, resulting in failure, instead of reconfiguration after relaxation.^{27,43} To avoid forming defects during



the surface functionalization, the hydrogenation density is controlled to not exceed 0.5.

Results and discussion

Functionalized CNT origami

Figure 2a shows the schematic of the surface functionalized CNT-O by hydrogen atoms. The hydrogenation is applied to the carbon atoms within the area marked by yellowish solid lines on the outside of the CNT to generate mountain folds. On the inside of the CNT, the hydrogen atoms are placed on the top of carbon atoms within the area enclosed by the yellowish dashed lines to generate valley folds. After the full relaxation in MD simulation, the functionalized CNT reaches a minimum-energy equilibrium state, transforming a CNT into a CNT-O with well-known Miura-ori

origami patterns characterized by crease lengths ($a = 79.577 \text{ \AA}$ and $b = 115.62 \text{ \AA}$), acute angle between creases ($\beta = 30^\circ$), and folding width (t), as shown in Figure 2a. The detailed relaxation process of hydrogenated CNT in MD simulation can be found in Supplementary information Figure S3. The hydrogenation formed sp^3 carbon-hydrogen bonds induces local bending, which is affected by the folding width (t) and the hydrogenation density (ρ is defined as the ratio between the number of hydrogen atoms and carbon atoms within the crease area), resulting in the shape morphing of CNT. Because the one-dimensional (1D) CNT has a cylinder-like architecture constructed from the rolling up of single-layer graphene with a nanometer-range diameter, the CNT-O can be considered to be formed by bending/rolling the graphene Miura-ori (Figure 2b). To understand the relationship between the diameter of CNT-O



and folding width, we assume the centerline length ($L+2t$) and the height (h) of the graphene Miura-ori cell does not change during the bending (Figure 2b). Hence the diameter of CNT-O is given by

$$D = \frac{n(L+2t)}{\pi} + h, \quad 6$$

where n is the number of graphene unit cells in CNT-O (e.g., $n=6$ in Figure 2b) and $L+2t$ is the length of the graphene Miura-ori unit cell. Figure 2b shows the schematic of the Miura-ori unit cell before bending/rolling. The outer dimensions of Miura-ori without considering the folding width t are then given by^{22,28}

$$L = 2b \sin(\varphi/2) \quad 7a$$

$$w = 2a \frac{\cos \beta}{\cos(\varphi/2)} \quad 7b$$

$$h = \frac{a \sqrt{\sin^2 \beta - \sin^2(\varphi/2)}}{\cos(\varphi/2)}, \quad 7c$$

where $\varphi \in [0^\circ, 2\beta]$ is the projection angle between two adjacent “valley” creases, characterizing the folding of the Miura-ori unit cell; $\varphi=0^\circ$ and 2β represent the completely collapsed and planar states, respectively. Considering the folding width t , the length and width of the graphene Miura-ori is $L+2t$ and $w+2t$ while h does not show a significant change (Figure 2b). Another two dihedral angles $\alpha_1, \alpha_2 \in [0^\circ, 180^\circ]$ can also characterize the geometry of Miura-ori, which are given by

$$\alpha_1 = \cos^{-1} \left[1 - 2 \frac{\sin^2(\varphi/2)}{\sin^2 \beta} \right] \quad 8a$$

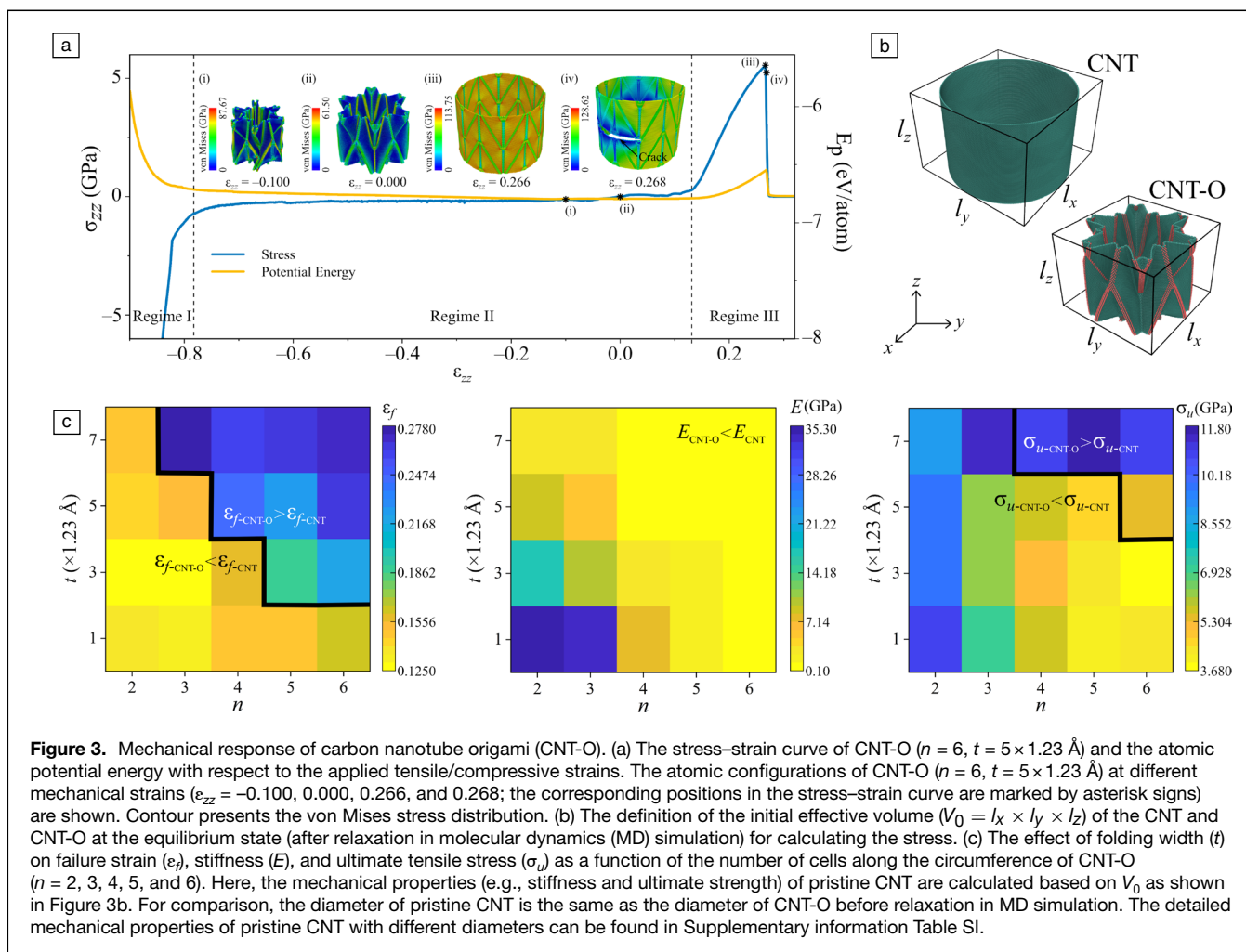
$$\alpha_2 = \cos^{-1} [1 - 2 \cot^2 \beta \tan^2(\varphi/2)]. \quad 8b$$

The dihedral angle (i.e., folding angle) in graphene origami is induced by hydrogenation, which is dependent on the folding width and hydrogenation density.²⁷ Based on Equations 6–8, we can theoretically obtain the diameter of CNT-O with a given cell number (n) and the dimension of graphene Miura-ori unit cell. For simplicity, the CNT-O characterized by (n, m) , where n is the number of the cells along the circumference of CNT-O and m means the folding thickness $t = m \times 1.23 \text{ \AA}$, is written as CNT-O (n, m) in the following text. Figure 2c shows the effect of folding width ($t = m \times 1.23 \text{ \AA}$, $m = 1, 3, 5, 7$, and 9) on CNT-O diameter for different cell numbers ($n = 2, 3, 4, 5$, and 6). The theoretical analysis and the simulation results show a good agreement except for the folding width $t = 9 \times 1.23 \text{ \AA}$. The deviation could emanate from (1) CNT-O cannot be completely collapsed/folded because of the van der Waals force between adjacent CNT origami panels; (2) rolling up the completely collapsed graphene Miura-ori to CNT-O could cause the unfolding of the creases, especially for limited cells (e.g., $n = 2$). Hence, the simulation results are

higher than the theory when $t = 9 \times 1.23 \text{ \AA}$, as shown in Figure 2c. In addition, defects are found near the creases during the relaxation process when $t = 9 \times 1.23 \text{ \AA}$ (see Supplementary information Figure S5). Hence, the CNT-O with folding thickness $t = 9 \times 1.23 \text{ \AA}$ is excluded in the following study. Considering the effect of hydrogen density on the CNT-O diameter, the hydrogen atoms within the crease region are deleted randomly to generate creases with different hydrogen densities ($\rho = 0.1, 0.2, 0.3, 0.4$, and 0.5). Results in Figure 2d show that the diameter of CNT-O ($n = 5$) decreases with the increased hydrogen density for all folding widths. To better present the variation of the diameter with the increased hydrogenation density when folding width $t = 1 \times 1.23 \text{ \AA}$ and $3 \times 1.23 \text{ \AA}$, we plot these two folding widths for different hydrogenation densities with a fine range in Figure 2d.

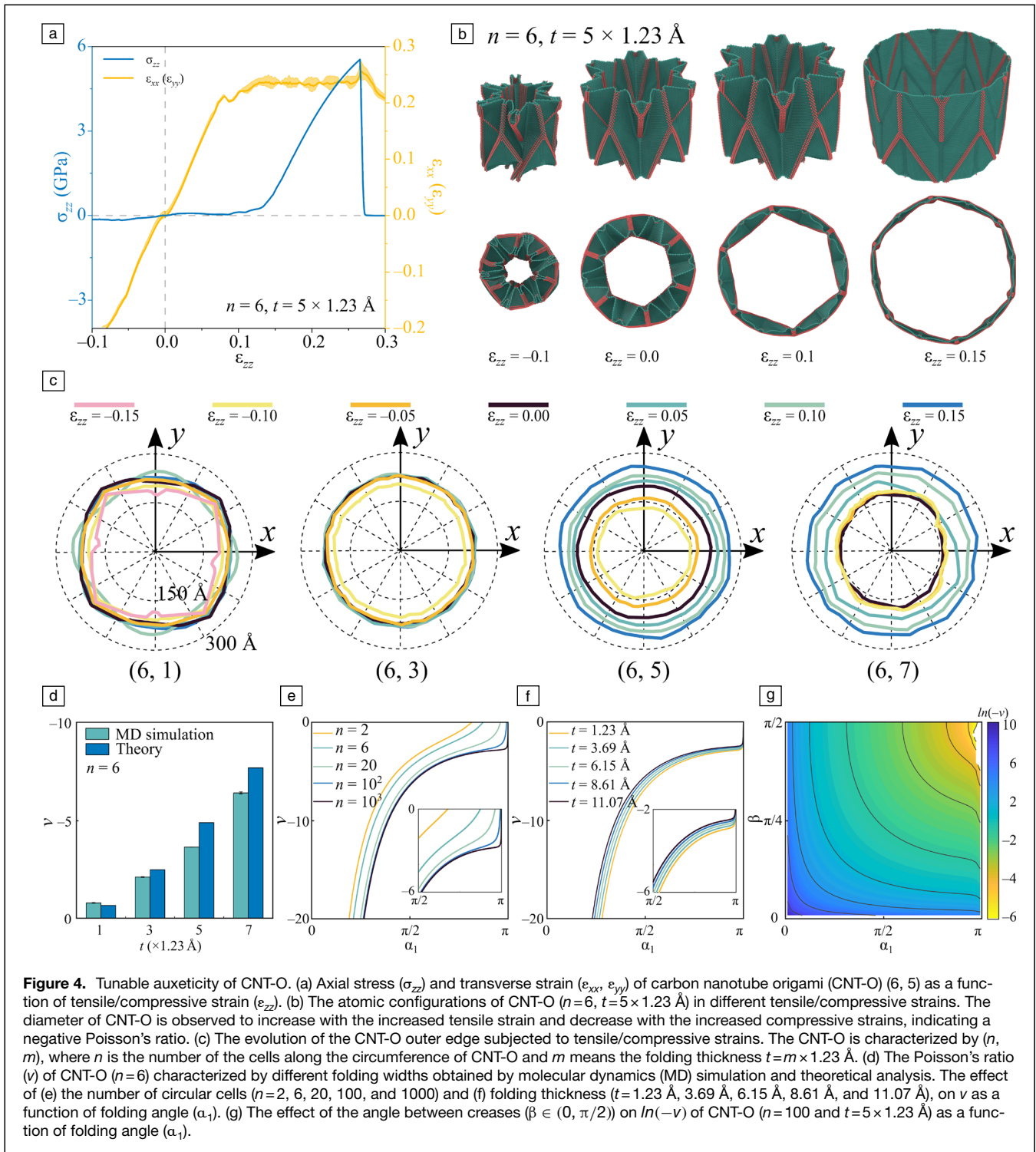
Mechanical properties of CNT origami

After obtaining the stable CNT-O by surface functionalization, we further study the effect of folding widths (t) and numbers of the cells (n) on the mechanical response of CNT-O. Figure 3a shows a typical stress–strain response and mechanical deformation of CNT-O (6, 5) upon uniaxial compression/tension in the z -direction. We also show the atomic configurations of CNT-O at different mechanical strains ($\epsilon_{zz} = -0.100, 0.000, 0.266$, and 0.268) in Figure 3a. Here, we need to clarify the CNT/CNT-O stress calculation. As shown in Equation 1, the axial stress is calculated by averaging the virial stress of all atoms in the system. Hence, the definition of V_0 is critical for stress calculation. To compare the mechanical properties between CNT-O and CNT, $V_0 = l_x l_y l_z$ is defined as the volume of the outside cuboid of the CNT/CNT-O unit cell at the equilibrium state (see Figure 3b and Supplementary information Figure S6). In addition, the corresponding CNT shares the same diameter with the CNT-O before relaxation (Supplementary information Figure S6). Three distinct regimes can characterize the CNT-O stress–strain response: the densification of CNT-O in compression (Regime I); a plateau stress regime caused by the folding/unfolding of creases and the bucking (e.g., (i) in Figure 3a) of CNT-O panels in compression (Regime II); and the stretching of carbon atomic bonds (e.g., (iii) in Figure 3a) in tension (Regime III). It is found that the stress increases slightly with increased strain in Regime II; also, the potential energy of CNT-O seems unchanged in this regime, indicating the low stiffness of CNT-O. Further observation of the von Mises stress distribution in CNT-O (see atomic configurations in Figure 3a) finds that the stress is concentrated in origami creases, revealing that the low stiffness results from the hydrogenated creases (e.g., (iii) in Figure 3a). Finally, the crack forms at the junction of creases and propagates rapidly, leading to a brittle failure of CNT-O ((iv) in Figure 3a). We also apply cycle tensile loading/unloading on CNT-O in Supplementary information Figure S7; the overlapped stress–strain responses imply that the deformation of CNT-O is reversible, and CNT-O has excellent mechanical resilience.



Next, we turn our attention toward three specific mechanical values (i.e., failure strain ϵ_f , stiffness E , and ultimate strength σ_u) to evaluate the mechanical properties of CNT-O in Figure 3c. The detailed mechanical properties of pristine CNT can be found in Supplementary information Table SI. The surface functionalization-induced origami feature increases the stretchability through the unfolding of creases. In contrast, hydrogenation also causes stress concentration (see Figure 3a), decreasing the failure strain. Hence, the tradeoff between the unfolding of creases and the stress concentration determines the failure strain of CNT-O. Compared with the pristine CNT, the stretchability of CNT-O is increased in the case of samples with more cells (n) and large folding width (t). In general, the failure strain of CNT-O increases with increased folding width and number of cells along the circumference of CNT-O. Because the stiffness of CNT-O is related to the unfolding of the creases subjected to tension, the stiffness of CNT-O is much smaller than that of pristine CNT (Figure 3c). For example, the stiffness of CNT-O (2,7) is 3.373 GPa, while the stiffness of the corresponding CNT is 107.046 GPa. It is worth mentioning that this stiffness is calculated based on the volume of the outside cuboid, which varies with the diameter of the CNT. If the stiffness of CNT is

calculated based on the volume of the cylinder, the calculated stiffness is 899.108 GPa and independent of the CNT diameter (see Supplementary information Figure S6 and Table SI). Interestingly, the stiffness of CNT-O shows an opposite trend with increased folding width and number of cells along the circumference of CNT-O compared to the trend of the failure strain. We also report the ultimate strength of CNT-O in Figure 3c. In the case of samples with more cells (n) and large folding width (t), the ultimate strength of CNT-O is found to be even higher than that of CNT due to the decreased initial volume (V_0) induced by hydrogenation. In return, the hydrogenation of carbon atoms causes the stress concentration around creases (Figure 3a), resulting in the decreased strength in most cases of CNT-O. It is worth mentioning that the ultimate strength of CNT-O does not show a clear trend to the variable parameters (t and n) compared to the contour plots of failure strain and stiffness. It is due to that the stress calculation is dependent on the effective cross-sectional area of CNT-O, and both parameters (t and n) show a nonlinear relationship between the diameter of CNT-O (Figure 2c). Generally, CNT-O can realize the increase of stretchability and strength simultaneously through geometrical parameter engineering.



Tunable auxeticity of CNT-O

The most interesting property of the Miura-ori-related structures is the strain-dependent negative Poisson's ratio.^{22,49}

Figure 4a presents the axial stress and transverse strain of CNT-O (6, 5) as a function of loading strain. The error area shown in the yellow curve in Figure 4a results from the difference between the transverse strain of CNT-O (6, 5) in the

x - and y -directions. To better exhibit the auxeticity of CNT-O, the atomic configurations of CNT-O (6, 5) in different tensile/compressive strains are shown in Figure 4b. The diameter of CNT-O (6, 5) is found increased with the increased tensile strains and decreased with the increased compressive strains, indicating a negative Poisson's ratio of CNT-O. Figure 4c shows the outer edge of CNT-O characterized by different



folding widths under certain strains. In addition to the negative Poisson's ratio of CNT-O observed in Figure 4c, the change of the CNT-O diameter is more evident in samples with larger folding width (i.e., CNT-O (6, 7)), indicating that the Poisson's ratio of CNT-O decreases with the increased folding width. Moreover, the distance between the adjacent outer edge is variable, which seems to decrease with the increased tensile strains, revealing the strain-dependent Poisson's ratio of CNT-O.

To better understand the auxeticity of CNT-O, we calculate the Poisson's ratio of CNT-O theoretically. Assuming that the panels that constitute CNT-O are rigid, the thickness of CNT-O is neglected, and the creases are ideal (the stiffness of creases is much smaller than that of panels), the Poisson's ratio (ν), defined as the ratio between the strains in the transverse direction and the loading direction, is given by

$$\nu = -\frac{dD/D}{d(w+2t)/(w+2t)}, \quad 9$$

where dD and $d(w+2t)$ refer to the derivations of the diameter and height of CNT-O, respectively. Based on Equations 6 and 7b, dD/D and $d(w+2t)/(w+2t)$ can be obtained as

$$\frac{dD}{D} = \left\{ \frac{bn \cos(\varphi/2)}{\pi D} - \frac{a \sin(\varphi/2) \cos^2(\beta)}{2D \cos^2(\varphi/2) \sqrt{\sin^2 \beta - \sin^2(\varphi/2)}} \right\} d\varphi \quad 10a$$

$$\frac{d(w+2t)}{(w+2t)} = \frac{a \cos(\beta) \sin(\varphi/2)}{2 \cos(\varphi/2) [a \cos \beta + t \cos(\varphi/2)]} d\varphi. \quad 10b$$

Substituting Equation 8a into Equations 10a and 10b, the Poisson's ratio of CNT-O characterized by different geometrical parameters (a , b , β , t , and n) can be expressed as a function of dihedral angle α_1 ($\alpha_1 \in (0^\circ, 180^\circ)$). $\alpha_1 = 0^\circ$ and 180° represent the completely collapsed state and the completely unfolded state, respectively. Figure 4d displays the Poisson's ratio of CNT-O ($n=6$) characterized by different folding widths obtained by theoretical analysis and MD simulation. The MD results are obtained by calculating the slope of the transverse-loading strain of CNT-O in the strain interval from -1 percent to 1 percent. The theoretical results are calculated based on Equations 8a, 9, and 10 with certain dihedral angle α_1 of the corresponding CNT-O at the equilibrium state. Both the theory and the simulation show that Poisson's ratio decreases with the increased folding thickness. The deviation between the theory and simulation results from three aspects: (1) The theory of the Poisson's ratio is driven based on the assumption of the rigid panel in CNT-O while panels of CNT-O are flexible/deformable in MD simulation; (2) the effective thickness of CNT-O cannot be neglected when α_1 is too small (i.e., large folding thickness in Figure 4d); and (3) with a limited number of cells (n) along the circumference of CNT-O, the determination of the dihedral angle α_1 in 3D space loses accuracy

with decreased folding width. This inaccuracy of α_1 can also be observed in Figure 4e when discussing the effect of n on the Poisson's ratio of CNT-O. The Poisson's ratio equals zero, meaning that the CNT-O is in a completely unfolded state. In the theoretical analysis, this state is reached when $\alpha_1 = 180$ degrees. However, we find that the α_1 is smaller than 180 degrees when the Poisson's ratio of CNT-O is zero for the sample with small n (e.g., $n=2, 6$, and 20 in Figure 4e). This is because the Miura-ori unit cells of CNT-O with limited n are in a curved shape when the origami creases are unfolded. It is also found in Figure 4e that the Poisson's ratio of CNT-O increases with the decreased n at the same α_1 . Figure 4f shows the effect of folding thickness on the CNT-O's Poisson's ratio ($n=100$ and $\beta=30^\circ$), which increases with the increased folding thickness at the same α_1 . In Figure 4g, we show the effect of β on the Poisson's ratio of CNT-O ($n=100$ and $t=5 \times 1.23 \text{ \AA}$) at different α_1 and find that the Poisson's ratio of CNT-O increases with the increased α_1 and β .

Scale-independent auxeticity

To further understand the scale-independent Poisson's ratio of the Miura-ori tube, we fabricate the Miura-ori tube structures out of the paper. In the manufacturing process shown in Figure 5a, the creases of Miura-ori patterns are first introduced by laser cutting (Trotec, Speedy 100) with dotted lines (characterized by geometrical parameters a , b , and β) followed by the hand-folded Miura-ori sheet. The Miura-ori tubes are then fabricated by rolling the Miura-ori sheet and attaching their two opposite edges to each other with glue. Three samples characterized by $a=b=25$ mm, and $\beta=45^\circ, 60^\circ$, and 75° , comprising 15×5 Miura-ori unit cells (15 unit cells and 5 layers along the circumference and the axial directions of the tube, respectively) are fabricated, as shown in Figure 5b-d. To study the auxeticity property of Miura-ori tubes, the Miura-ori tubes are first placed in a completely collapsed state and fixed at the two ends by the grippers of a uniaxial tensile test machine (ADMET, eXpert 8612) ((I) in Figure 5b-d). Then the top gripper goes up slowly, and the deformations of Miura-ori tubes are recorded using a digital camera (Sony RX100IV). The snapshots of Miura-ori tubes subjected to certain deformation strains are shown in Figure 5b-d. It is found clearly that the Miura-ori tubes expand significantly with the increased strains (i.e., the increased axial length). Here, the axial length of Miura-ori tubes (W) is directly read from the testing machine whereas the diameter (D) is obtained by averaging the three-time tests of the central layer (e.g., (I) in Figure 5b-d). Such scale-independent auxeticity response of Miura-ori tubes can be characterized and predicted by the kinematics of the folding/unfolding, as concluded in Equations 9 and 10. However, considering the limited unit cells in the axial direction of Miura-ori tubes and the effect of the tail,⁵⁰ the axial length (W) is given by

$$W = 2qa \frac{\cos \beta}{\cos(\varphi/2)} + b \cos(\varphi/2), \quad 11$$

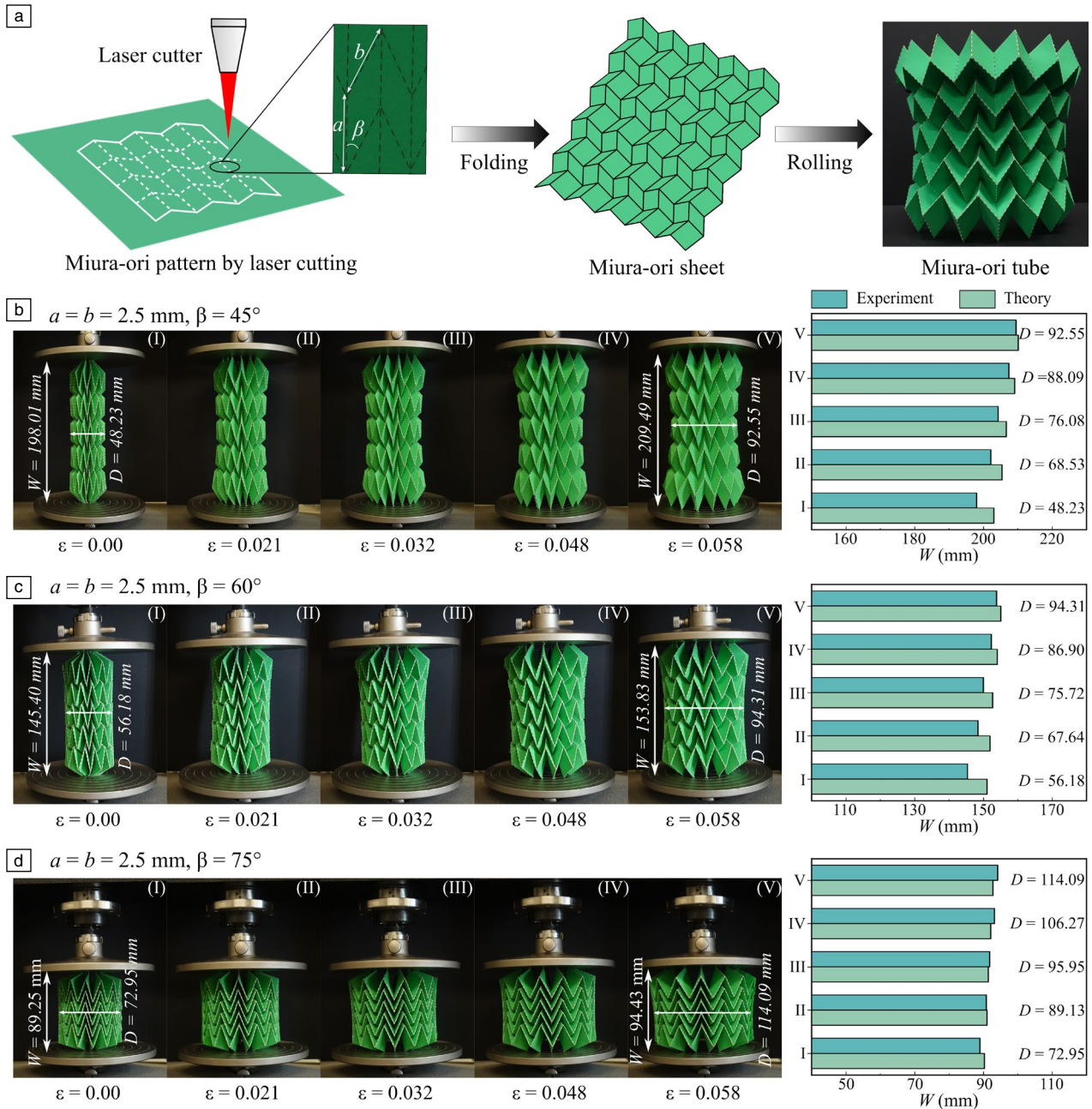


Figure 5. The experiment of Miura-ori tubes. (a) The manufacturing process of a Miura-ori tube made out of paper that includes laser cutting, hand folding, and rolling. The auxeticity of Miura-ori tubes characterized by $a=b=25 \text{ mm}$, and (b) $\beta=45^\circ$, (c) $\beta=60^\circ$, and (d) $\beta=75^\circ$, obtained by experimental test and theoretical analysis. The column values inside the right graph represent the diameter (D) of Miura-ori tubes. For each sample at certain strains, the diameter of the Miura-ori tube is tested for three times. The experimental and theoretical results indicate the scale-independent and strain-dependent negative Poisson's ratio of the Miura-ori tube.

where q represents the layer of the Miura-ori cells along the axial direction of the Miura-ori tube and $q=5$ in all three samples. The diameter of Miura-ori tubes with different axial lengths (i.e., subjected to different strains) can be predicted by Equations 6 and 11 with $t=0$. As shown in Figures 5b–d, we find a good agreement between the theoretical predictions and experimental results, which reveals

the scale-independent auxeticity of Miura-ori tubes. The deviation between the theory and experiments results from three main factors: (1) the defects/imperfection introduced during the fabrication (i.e., hand folding and rolling); (2) the boundary condition effect resulting from the limited layers of cells along axial direction; and (3) error in measuring the diameter of samples.



Concluding remarks

In summary, we have combined MD simulation and theoretical analysis to demonstrate that the surface functionalization-assisted origami strategy imparts a new platform for designing CNT metamaterials with tunable mechanical properties. Specifically, we have shown that altering the folding width, topological parameters of Miura-ori patterns, and the number of cells along the circumference of Miura-ori CNTs can tune stiffness, ultimate strength, failure strain, and the range of attainable negative Poisson's ratios. Our results demonstrate that applying mechanical strains can further tune Poisson's ratio of hydrogenated CNT-O. Additionally, comparing the experimental results of a Miura-ori tube made by folding/rolling a paper at the macroscale and the atomic scale numerical simulation results for nanoscale origamis confirms that the strain-dependent negative Poisson's ratio governed by the kinematics of the crease folding/unfolding is scale-independent, and can be well predicted by the proposed continuum theory. By systematic design of CNT-O, we are not only able to enhance the mechanical properties (i.e., failure strain and ultimate strength in some cases) and achieve exotic properties (e.g., negative Poisson's ratio), but we can also tailor the underlying architectural parameters (e.g., a , b , β , t , and n) to engineer and program the properties of CNTs. The present study provides new opportunities for the realization of the next generation of low-dimensional nanomaterials capable of achieving tunable mechanical properties and auxeticity for applications in wearable nanoelectronics and soft nanorobots.

Acknowledgments

This research was undertaken, in part, thanks to funding from the Canada Research Chairs program to A.H.A. in Multifunctional Metamaterials. A.H.A. also acknowledges the financial support by the Natural Sciences and Engineering Research Council of Canada through NSERC Discovery Grant (RGPIN-2022-04493) and the Canada Foundation for Innovation (CFI) through the John R. Evans Leaders Fund. J.C. acknowledges the financial support provided by the China Scholarship Council (File No. 201909370077), Quebec Research Fund - Nature and Technologies (FRQNT) doctoral awards (B2X), and McGill University. This research was enabled by support from Calcul Québec and Compute Canada.

Data availability

The data will be made available upon reasonable request.

Conflict of interest

On behalf of all authors, the corresponding author states that there is no conflict of interest.

Supplementary information

The online version contains supplementary material available at <https://doi.org/10.1557/s43577-023-00545-0>.

References

1. Y. Gogotsi, *MRS Bull.* **40**(12), 1110 (2015)
2. S.Y. Kim, J.C. Lee, G. Seo, J.H. Woo, M. Lee, J. Nam, J.Y. Sim, H.R. Kim, E.C. Park, S. Park, *Small Sci.* **2**, 2100111 (2022)
3. Z. Komeily-Nia, L.-T. Qu, J.-L. Li, *Small Sci.* **1**(2), 2000026 (2020). <https://doi.org/10.1002/smssc.202000026>
4. B. Ni, D. Steinbach, Z. Yang, A. Lew, B. Zhang, Q. Fang, M.J. Buehler, J. Lou, *MRS Bull.* **47**(8), 848 (2022)
5. T. Cui, S. Mukherjee, P.M. Sudeep, G. Colas, F. Najafi, J. Tam, P.M. Ajayan, C.V. Singh, Y. Sun, T. Filleter, *Nat. Mater.* **19**, 405 (2020). <https://doi.org/10.1038/s41563-019-0586-y>
6. A. Kis, G. Csanyi, J.P. Salvetat, T.N. Lee, E. Couteau, A.J. Kulik, W. Benoit, J. Brugger, L. Forro, *Nat. Mater.* **3**, 153 (2004)
7. M. Guo, Y. Qian, H. Qi, K. Bi, Y. Chen, *Carbon* **157**, 185 (2020)
8. T.W. Odom, J.-L. Huang, P. Kim, C.M. Lieber, *Nature* **391**, 62 (1998)
9. N. Hamada, S. Sawada, A. Oshiyama, *Phys. Rev. Lett.* **68**, 1579 (1992)
10. J. Wu, H. Ma, P. Yin, Y. Ge, Y. Zhang, L. Li, H. Zhang, H. Lin, *Small Sci.* **1**(4), 2000053 (2021). <https://doi.org/10.1002/smssc.202000053>
11. A. Peigney, C. Laurent, E. Flahaut, R.R. Bacsa, A. Rousset, *Carbon* **39**, 507 (2001)
12. C. Zhang, A. Akbarzadeh, W. Kang, J. Wang, A. Mirabolghasemi, *Carbon* **131**, 38 (2018)
13. J. Cai, A. Akbarzadeh, *Mater. Des.* **206**, 109811 (2021). <https://doi.org/10.1016/j.matdes.2021.109811>
14. J. Cai, H. Chen, Y. Li, A. Akbarzadeh, *Small Sci.* **2**(12), 2270024 (2022). <https://doi.org/10.1002/smssc.202270024>
15. H. Zhan, G. Zhang, J.M. Bell, V.B.C. Tan, Y. Gu, *Nat. Commun.* **11**, 1905 (2020)
16. E. Pop, V. Varshney, A.K. Roy, *MRS Bull.* **37**(12), 1273 (2012)
17. G.S. Jung, M.J. Buehler, *Nano Lett.* **18**, 4845 (2018)
18. Z. Yang, M.J. Buehler, *Small Methods* **6**, 84 (2022)
19. A. Pedrielli, S. Taioli, G. Garberoglio, N.M. Pugno, *Carbon* **132**, 766 (2018)
20. Y. Zhu, Y. Wang, B. Wu, Z. He, J. Xia, H. Wu, *Nano Lett.* **21**, 8401 (2021)
21. T.C. Shyu, P.F. Damasceno, P.M. Dodd, A. Lamoureux, L. Xu, M. Shlian, M. Shtein, S.C. Glotzer, N.A. Kotov, *Nat. Mater.* **14**, 785 (2015)
22. M. Schenk, S.D. Guest, *Proc. Natl. Acad. Sci. U.S.A.* **110**, 3276 (2013)
23. L. Yuan, H. Dai, J. Song, J. Ma, Y. Chen, *Mater. Des.* **189**, 108494 (2020)
24. S. Li, H. Fang, S. Sadeghi, P. Bhovad, K.W. Wang, *Adv. Mater.* **31**, e1805282 (2019)
25. S.J.P. Callens, A.A. Zadpoor, *Mater. Today* **21**, 241 (2018)
26. P.M. Reis, F. Lopez Jimenez, J. Marthelot, *Proc. Natl. Acad. Sci. U.S.A.* **112**, 12234 (2015)
27. J. Cai, E. Estakhrihaghghi, A. Akbarzadeh, *Carbon* **191**(5696), 610 (2022). <https://doi.org/10.1016/j.carbon.2022.02.008>
28. Z.Y. Wei, Z.V. Guo, L. Dudte, H.Y. Liang, L. Mahadevan, *Phys. Rev. Lett.* **110**, 215501 (2013)
29. E. Boatti, N. Vasios, K. Bertoldi, *Adv. Mater.* **29**, 1700360 (2017)
30. D. Melancon, B. Gorissen, C.J. Garcia-Mora, C. Hoberman, K. Bertoldi, *Nature* **592**, 545 (2021)
31. Z. Zhai, Y. Wang, K. Lin, L. Wu, H. Jiang, *Sci. Adv.* **6**(47), eabe2000 (2020). <https://doi.org/10.1126/sciadv.abe2000>
32. B. Trembl, A. Gillman, P. Buskohl, R. Vaia, *Proc. Natl. Acad. Sci. U.S.A.* **115**, 6916 (2018)
33. B.N. Khare, M. Meyyappan, J. Kralj, P. Wilhite, M. Sisay, H. Imanaka, J. Koehne, C.W. Baushchlicher, *Appl. Phys. Lett.* **81**, 5237 (2002)
34. D.C. Elias, R.R. Nair, T.M. Mohiuddin, S.V. Morozov, P. Blake, M.P. Halsall, A.C. Ferrari, D.W. Boukhvalov, M.I. Katsnelson, A.K. Geim, K.S. Novoselov, *Science* **323**, 610 (2009)
35. B.N. Khare, M. Meyyappan, A.M. Cassell, C.V. Nguyen, J. Han, *Nano Lett.* **2**, 73 (2001)
36. S. Pekker, J.P. Salvetat, E. Jakob, J.M. Bonard, L. Forró, *J. Phys. Chem. B* **105**, 7938 (2001)
37. G. Zhang, P. Qi, X. Wang, Y. Lu, D. Mann, X. Li, H. Dai, *J. Am. Chem. Soc.* **128**, 6026 (2006)
38. A.V. Talyzin, S. Luzan, I.V. Anoshkin, A.G. Nasibulin, H. Jiang, E.I. Kauppinen, V.M. Mikoushkin, V.V. Shnitov, D.E. Marchenko, D. Noreus, *ACS Nano* **5**, 5132 (2011)
39. Z. Sun, C.L. Pint, D.C. Marcano, C. Zhang, J. Yao, G. Ruan, Z. Yan, Y. Zhu, R.H. Hauge, J.M. Tour, *Nat. Commun.* **2**, 559 (2011)
40. S. Plimpton, *J. Comput. Phys.* **117**(1), 1 (1995)
41. A. Stukowski, *Model. Simul. Mater. Sci. Eng.* **18**, 015012 (2010)
42. F. Müller-Plathe, *J. Chem. Phys.* **106**, 6082 (1997)
43. S. Zhu, T. Li, *ACS Nano* **8**, 2864 (2014)
44. D.T. Ho, V.H. Ho, V. Babar, S.Y. Kim, U. Schwingschlogl, *Nanoscale* **12**, 10172 (2020)
45. J. Mu, C. Hou, H. Wang, Y. Li, Q. Zhang, M. Zhu, *Sci. Adv.* **1**, e1500533 (2015)
46. L. Liu, Y. Liu, X. Li, N. Liu, B. Cui, X. Huang, *Phys. Status Solidi B* **256**, 1900095 (2019)
47. Q. Lu, M. Arroyo, R. Huang, *J. Phys. D Appl. Phys.* **42**, 102002 (2009)
48. X. Shi, B. Peng, N.M. Pugno, H. Gao, *Appl. Phys. Lett.* **100**, 191913 (2012)



49. K. Liu, P.P. Pratapa, D. Misseroni, T. Tachi, G.H. Paulino, *Adv. Mater.* **34**, e2107998 (2022)
50. M. Eidini, G.H. Paulino, *Sci. Adv.* **1**, e1500224 (2015)

Publisher's note Springer Nature remains neutral with regard to jurisdictional claims in published maps and institutional affiliations.

Springer Nature or its licensor (e.g. a society or other partner) holds exclusive rights to this article under a publishing agreement with the author(s) or other rightsholder(s); author self-archiving of the accepted manuscript version of this article is solely governed by the terms of such publishing agreement and applicable law.